Energy Conversion and Management 213 (2020) 112835

Contents lists available at ScienceDirect

Energy Conversion and Management

journal homepage: www.elsevier.com/locate/enconman

Hybrid wind energy scavenging by coupling vortex-induced vibrations and galloping

Junlei Wang[a,b], Shanghao Gu[a], Chengyun Zhang[a], Guobiao Hu[b], Geng Chen[b], Kai Yang[c,*], Hang Li[a], Yuyang Lai[d], Grzegorz Litak[e], Daniil Yurchenko[f]

[a] School of Mechanical and Power Engineering, Zhengzhou University, Zhengzhou 450000, China
[b] Department of Mechanical Engineering, The University of Auckland, Auckland, New Zealand
[c] School of Aerospace Engineering, Huazhong University of Science and Technology, Wuhan 430074, China
[d] Soyotec Technologies Co., Ltd., Beijing 100176, China
[e] Department of Automation, Technical University of Lublin, PL-20-618 Lublin, Poland
[f] Institute of Mechanical, Process & Energy Engineering, Heriot-Watt University, Edinburgh EH14 4AS, UK

ARTICLE INFO

Keywords:
Piezoelectric energy scavenging
Vortex-induced vibration
Galloping
Cross-section design

ABSTRACT

This paper presents a hybrid piezoelectric wind energy scavenger with different cross-sectioned bluff bodies, to enhance the energy scavenging performance by coupling both the vortex-induced vibrations (VIV) and galloping phenomena. Theoretical, experimental and computational fluid dynamics (CFD) studies are conducted to investigate the energy scavenger performance with three combinations of the circular and square cross-sections corresponding to the different values of an attack angle. Both theoretical analysis and experimental results reveal that the aerodynamic coefficients (Strouhal number and galloping force coefficients) play key roles in the energy scavenging characteristics. Aerodynamic coefficients for the distinct bluff-body cross-sections and attack angles can significantly affect the energy scavenger performance. Experimental results show that compared to the conventional galloping-based energy scavenger and VIV-based energy scavenger, the piezoelectric wind energy scavenger with an appropriate cross-sectioned bluff body for an appropriate attack angle can bring together the advantages of both VIV and galloping. These benefits can lead to significant performance improvement for a wide range of wind speeds (e.g. up to 71% improvement of the maximum voltage output). Afterward, CFD studies of the vortex shedding mechanism around the bluff body are performed to interpret the observed performance improvement. The CFD studies corroborate that the appropriately designed cross-section and selected attack angles of the bluff body improve the nearby airflow feature, which strengthens the vibration of the piezoelectric wind energy scavenger, leading to the energy scavenging enhancement.

1. Introduction

The technology of scavenging energy from the ambient environment has been widely explored in the recent two decades [1–14]. To convert various forms of dynamic energy into the electrical energy, the electromagnetic [15,16], electrostatic [17], triboelectric [18,19], and piezoelectric [20–24] mechanisms can be used. The piezoelectric material has been one of the most extensively used ways due to the advantages of high power density and the ease of implementation [21].

In terms of the energy source type, the research can be classified into structural vibration, acoustic, thermo-acoustic and aero-elastic energy scavenging. e.g. random excitations [25], flow-induced vibrations [26–30], noises [31] or other nonlinear vibrations [32–34]. Aero-elastic energy scavenging harnesses the energy from the ubiquitous wind. The key to the aero-elastic energy scavenging lies in the generation of aero-elastic vibrations, which can be achieved based on the well-known vortex-induced vibration (VIV) and galloping phenomena. Using the aforementioned two types of aeroelastic vibration phenomena, researchers have proposed various VIV/galloping energy scavengers. A lot of efforts have been devoted to their performance enhancement. In particular, Allen and Smith [35] designed an “eel”-shaped piezoelectric membrane structure in the Von Karman vortex street to harvest energy generated from vortex shedding behaviors. It first-time demonstrated that resonance is a key factor during converting flow energy into electric energy. For a similar but modified design on VIV piezoelectric energy scavenger (VIVPES), Akaydin et al. [36] put the flexible piezoelectric cantilever behind a cylinder, which generated a shedding vortex street. It was found that the placing distance could

* Corresponding author.
E-mail address: kaiyang@hust.edu.cn (K. Yang).

https://doi.org/10.1016/j.enconman.2020.112835
Received 10 January 2020; Received in revised form 30 March 2020; Accepted 8 April 2020
Available online 22 April 2020
0196-8904/

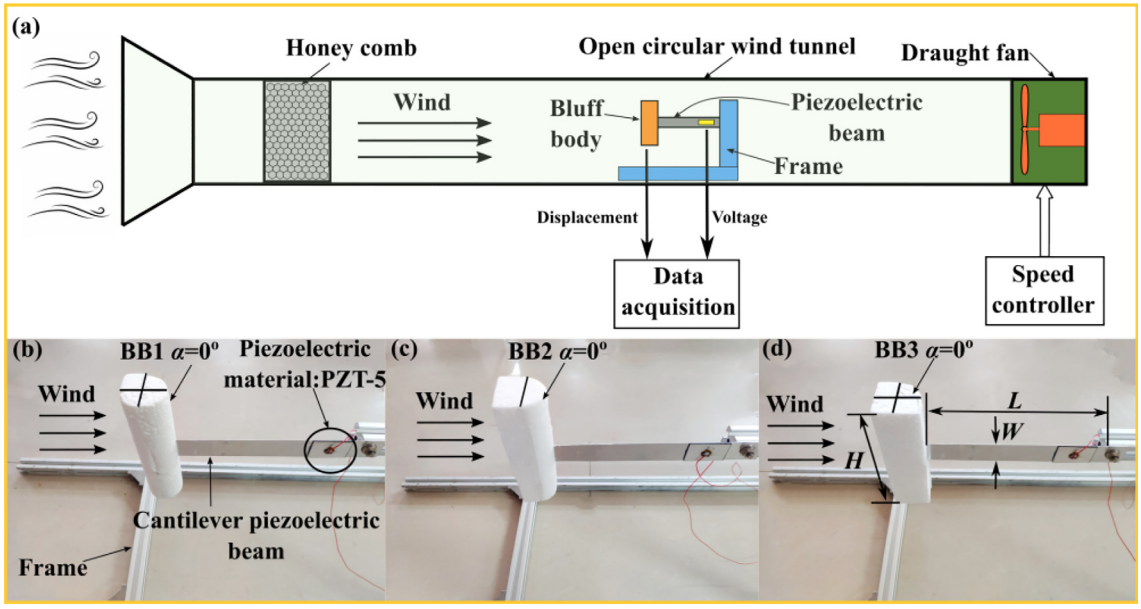

Fig. 1. The experimental device. (a) The overall sight of the wind tunnel test; (b)-(d): The built prototype with BB1 = 0°, BB2.α = 0° and BB3α = 0°

affect the voltage output. Mehmood et al. [37] built a computational fluid dynamic (CFD) simulation to study the performance of a VIVPES and identified three different regimes including pre-synchronization, synchronization, and post-synchronization during the aero-elastic vibration process. Then Dai et al. [38] further developed the theoretical model of a VIVPES using the Galerkin method and performed a parametric study to tune the related parameters for enhancing the performance of VIVPES in low freestream velocities. In conclusion, VIVPES is significantly proper for scavenging energy from low-speed flow for its low threshold flow speed [39,40]. However, the VIVPES performs well only in the lock-in region [41–44], because only when the vortex shedding frequency locks on the resonant frequency of the system, the vibration becomes significantly intense.

Galloping piezoelectric energy scavenger (GPES) has also been studied a lot for its high performance in higher operating wind speed as compared with VIVPES. Nuaimi et al. [45] proposed a phenomenological model of GPES to enhance the accuracy of the galloping model. Barrero et al. [46] established a mathematical model and comprehensively studied the instability of a GPES. Regarding the influence of the bluff body geometry, Abdelkefi et al. [47] performed the comparative study of the GPES with the bluff bodies possessing the square and triangular cross-sections. Yang et al. [48] conducted experiments to show the influence of the different side lengths of the bluff body's cross-section on the GPES performance. Yan et al. [49,50] discussed the performance improvement of the galloping energy scavenging by using a triangle bluff body. To enhance the performance of GPES, other researchers have designed prototypes to target at lower threshold flow speed and high-power outputs. The common methods include introducing nonlinearities [51–54], adding dismountable attachments [41], and using two degrees of freedom (2DOF) [55], etc. For example, Wang et al. [41] loaded the smooth cylinder with two Y-shaped attachments and transformed the original VIVPES into a GPES. Sun et al. [55] proposed a 2DOF GPES with a nested structure that is to improve the energy scavenging efficiency, and two combined bluff body-beam structure was experimentally investigated. Bibo et al. [51] introduced a nonlinear force to improve the performance of GPES. Hardening, softening and bistable forms of nonlinear force were studied. Tan et al. [56] presented the analytical solution of a low-wind speed galloping energy scavenger with a super-capacitor. It can be concluded that GPES often requires a higher threshold flow speed to induce the vibration, and aerodynamic damping plays the key role on the performance of GPES.

However, until now still few studies have been conducted to develop a flow-induced-vibration piezoelectric energy scavenger (FIVPES) that combines the advantages of VIVPES and GPES. Few researchers proposed the energy scavenging models by coupling VIV and galloping, e. g. He et al. [57] pointed out that the interaction of VIV and galloping could improve the FIVPES effectively by combining the VIV and galloping. The galloping regime could merge with the VIV regime during or after the lock-in region, which is significantly beneficial for energy scavenging by reducing the threshold flow speed. Using a cuboid bluff body, Yang et al. [58] proposed a VIV-galloping interactive PES and successfully established a distributed-parameter model. The key step in the modeling procedure was the determination of the coefficients of the aerodynamic damping using a semi-empirical approach. Sun et al. [59] proposed a series of D cross-sectional cylinders as the bluff body to induce both VIV and galloping and investigated the performance of energy scavenging. However, only the influence of a particular incoming wind attack angle on the VIV and galloping has been discussed. Qin et al. [60] used a crisscross beam to support two cuboid bluff bodies and a circular cylinder bluff body, to bring together both the galloping and VIV for its energy scavenging improvement. A traditional VIVPES often uses a regular cylinder-shaped bluff body, while a traditional GPES commonly uses a bluff body with corner features. However, using a bluff body that combines the cross-sections of both features (i.e., round and corner) has rarely been reported in the existing literature [57–59]. To comprehensively investigate the influence of various bluff bodies combining synergetic VIV and galloping behaviors, a hybrid energy scavenger from flow-induced vibrations is proposed in this paper. Using a novel bluff body with both round and corner features, a VIV and galloping interacted regime is generated for energy scavenging. Three different prototypes are fabricated and tested in a wind tunnel for the performance evaluation. Four different incoming wind attack angles are tested to investigate the influence of the attack angles on the performance. Subsequently, to accurately simulate the proposed hybrid energy scavenging that couples both the VIV and galloping, the mathematical model is numerically solved, and the numerical results are compared with those from the experiment. Finally, the flow field distribution is simulated through computational fluid dynamics (CFD) study using the Lattice-Boltzmann method (LBM), so as to give a visual demonstration of the performance enhancement of the proposed hybrid energy scavenger.

2. Design concept and experimental setup

In this section, we firstly introduce the experimental environment and the prototypes built. Fig. 1 (a–d) present the experimental setup and photos of the piezoelectric wind energy scavenger with three different combinations of the cross-sections of the bluff bodies, respectively. The piezoelectric wind energy scavenger consists of a cantilever piezoelectric beam, a bluff body fixed on a frame, which is mounted in the open-circuit circular wind tunnel (Diameter: 0.4 m). In the present experiment, by controlling the rotating speed of a draught fan different wind speeds can be produced. The honeycomb is used to stabilize the airflow in the tunnel. The data acquisition instrument records the vibrational displacement of the bluff body measured by a laser displacement sensor (LVC-TS800) and the voltage generated by the piezoelectric transducer (piezo-material: PZT-5). The piezoelectric beam is made of pure aluminum with the dimension of $L \times W \times h_b$=170 × 24 × 0.5 mm^3, where L, W and h_b are the beam length, width, and thickness, respectively.

Fig. 1 (b-d) presents the piezoelectric wind energy scavenger with three types of bluff bodies in this study. From left to right, they are defined as "BB1 $\alpha = 0^{\circ}$", "BB2 $\alpha = 0^{\circ}$" and "BB3 $\alpha = 0^{\circ}$", respectively. BB1 ~ BB3 represents the No.1 ~ No.3 cross-section shapes of the bluff body, whereas α represents the incoming wind attack angles. The detailed cross-section shapes of the bluff bodies are presented in Fig. 2. It is seen that BB1 is combined by a 3/4 cylinder and 1/4 cuboid, BB2 is combined by 1/2 cylinder and 1/2 cuboid, and BB3 is combined by 1/4 cylinder and 3/4 cuboid. For each bluff body, different wind attack angles α are investigated. The conventional cuboid and cylinder bluff bodies are presented as counterparts for performance comparison. The previous studies have proven that the energy scavenger with the cuboid bluff body mainly exhibits galloping, while the energy scavenger with the circular cylinder bluff body mainly exhibits vortex-induced vibration (VIV). In this study, the combinations of the circular and square cross-sections can bring together the advantages of both the VIV and galloping for energy scavenging enhancement. Therefore, this study intends to use the experimental and numerical study to find the optimal cross-sectioned bluff body. The dimension of each bluff body is $H \times D \times D$ = 118 ×32 × 32 mm^3. Note that, different bluff bodies may bring mass variations that affect the vibration of the piezoelectric beam. Therefore, for fair performance comparison, when changing the bluff bodies in the experiment, a small mass is added or removed to compensate for the mass difference to ensure the same mass of all the bluff bodies.

3. Mathematical modeling and experimental validation

In this section, to understand the dynamic insight of the coupled galloping vibration and VIV of the energy scavenger, the governing equations of the energy scavenger subjected to the VIV and galloping simultaneously are formulated. Afterward, the mathematical model is experimentally validated through wind tunnel tests.

3.1. Mathematical modeling

According to the schematic of the piezoelectric wind energy scavenger, the governing equations of the coupled galloping vibration and VIV of the energy scavenger can be formulated. The total kinetic energy and elastic potential energy of the energy scavenger is

$$T = \frac{1}{2}\int_0^D \rho_b\left(\dot{w}(L,t) + \xi\frac{\partial \dot{w}(L,t)}{\partial z}\right)^2 d\xi + \frac{1}{2}\int_0^L \rho_L(\dot{w}(z,t))^2 dz \tag{1}$$

$$V_p = \frac{1}{2}\int_0^L EI\left(\frac{\partial^2 w(z,t)}{\partial z^2}\right)^2 dz - \int_{z_{p1}}^{z_{p2}} J_p\frac{\partial^2 w(z,t)}{\partial z^2} V dz + \frac{1}{2}C_p V^2 \tag{2}$$

where $w(z,t)$ is the deflection displacement of the piezoelectric beam at position z and time t. $\dot{w} = \partial w/\partial t$. $\rho_b = \rho_b(\xi)$, $\rho_L = \rho_L(z)$ are the bluff body mass per unit length at position ξ and the beam mass per unit length at position z, respectively. EI is the bending stiffness of the piezoelectric beam including the contribution of both the beam and the piezoelectric transducer. J_p is the electromechanical term of the piezoelectric transducer [21]. C_p, V are the internal capacitance and voltage output of the piezoelectric transducers, respectively. The piezoelectric transducer is in the range of $[z_{p1}, z_{p2}]$ on the beam.

Since the first-mode vibration is dominant for the energy scavenging, assume that $w(z,t) = \phi_1(z)q_1(t)$, where $\phi_1(z)$ is the first-mode

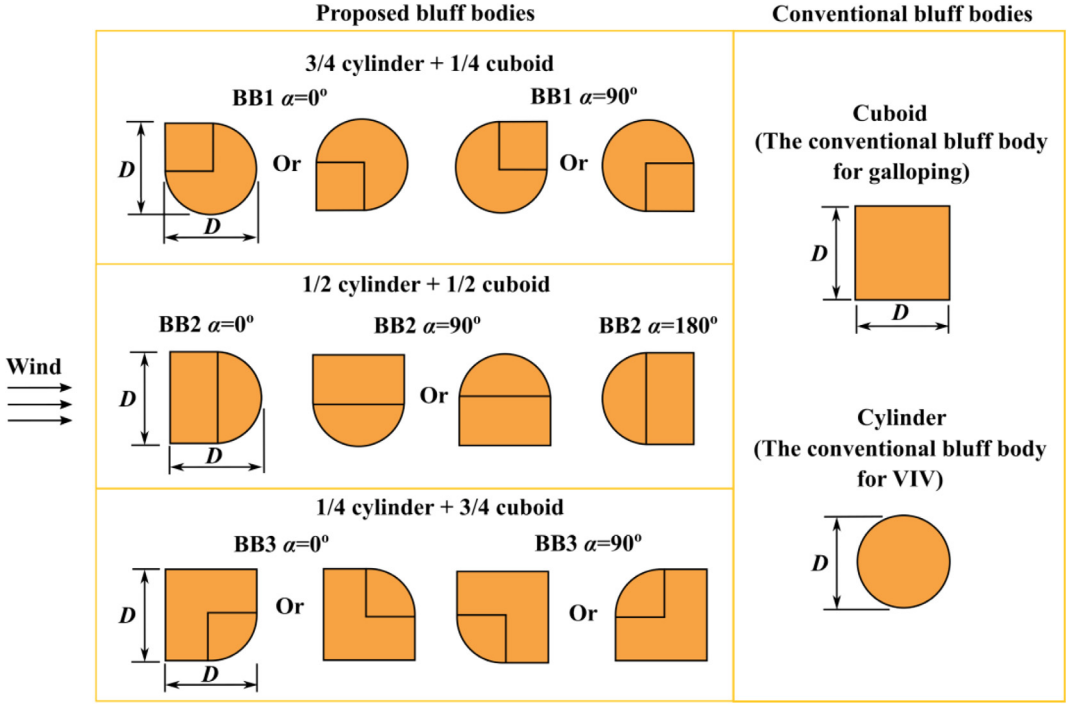

Fig. 2. The schematic of the test cases: different cross-sectioned bluff bodies and different wind attack angles.

shape function, $q_1(t)$ is the first-model coordinate. Therefore,

$$T = \frac{1}{2}M_{eff}\dot{q}_1^2 \tag{3}$$

$$V_p = \frac{1}{2}K_{eff}q_1^2 + \Theta_1 q_1 V + \frac{1}{2}C_p V^2 \tag{4}$$

where

$$\phi_1(L) + 0.5D\frac{d\phi_1(L)}{dz} = 1 \tag{5}$$

$$M_{eff} = \int_0^D \rho_b\left(\phi_1(L) + \xi\frac{d\phi_1(L)}{dz}\right)^2 d\xi + \int_0^L \rho_L\phi_1^2(z)dz \tag{6}$$

$$K_{eff} = \int_0^L EI\left(\frac{d^2\phi_1(z)}{dz^2}\right)^2 dz \tag{7}$$

$$\Theta_1 = -\int_{z_{p1}}^{z_{p2}} J_p\frac{d^2\phi_1(z)}{dz^2}dz \tag{8}$$

The virtual work done of the fluid force F_a acting on the bluff body is

$$\delta W_p = F_a\delta\left[w(L,t) + 0.5D\frac{\partial w(L,t)}{\partial z}\right] = F_a\delta q_1 \tag{9}$$

When considering both the galloping vibration and VIV, the fluid force F_a can be expressed as follows [58],

$$F_a = \frac{1}{2}\rho U^2 DH\left[-f\left(\psi + \frac{\dot{q}_1}{U}\right) + C_{Fy}\right] \tag{10}$$

where U is the incoming wind speed. f is the aerodynamic constant related to the shape of the bluff body. ρ is air density. ψ is the angular displacement related to the VIV of the energy scavenger. C_{Fy} is the aerodynamic force coefficient related to the galloping vibration of the energy scavenger, which is determined by the experiments. According to Yang et al. [58], ψ and C_{Fy} can be expressed as follows,

$$\ddot{\psi} + 2\zeta\omega_{VIV}\left[\left(\frac{2f}{C_{L0}}\right)^2\psi^2 - 1\right]\dot{\psi} + \omega_{VIV}^2\left(\psi + \frac{\dot{q}_1}{U}\right) = -\frac{\ddot{q}_1}{H + 0.5D} \tag{11}$$

$$C_{Fy} = \sum_{i=1}^{7} A_i\left(\frac{\dot{q}_1}{U}\right)^i (i = 1, 3, 5, 7) \tag{12}$$

where Eq. (11) is the wake oscillator of the VIV. ζ, ω_{VIV} are the damping ratio and the vortex shedding frequency for the VIV. $A_i(i = 1, 3, 5, 7\cdots)$ are the galloping force coefficients. C_{L0} is the amplitude of the fluctuating lift coefficient of the stationary bluff body.

$$\zeta = \frac{Df}{2\sqrt{2}\pi^2 H} \tag{13}$$

$$\omega_{VIV} = \frac{2\pi US_t}{D} \tag{14}$$

where S_t is the Strouhal number. Note that different shapes of the bluff body lead to different S_t and $A_i(i = 1, 3, 5, 7)$, and therefore they are identified experimentally.

Furthermore, assuming that the equivalent first-mode damping of the piezoelectric beam is C_{eff}, based on Lagrange equations, the governing equations of the energy scavenger subjected to coupled galloping vibration and VIV are presented as follows,

$$M_{eff}\ddot{q}_1 + C_{eff}\dot{q}_1 + K_{eff}q_1 + \Theta_1 V = \frac{1}{2}\rho U^2 DH\left[-f\left(\psi + \frac{\dot{q}_1}{U}\right) + C_{Fy}\right] \tag{15}$$

When the piezoelectric transducer connects a resistor R, the following electrical equation is obtained.

$$\frac{V}{R} + C_p\dot{V} = \Theta_1\dot{q}_1 \tag{16}$$

By defining

$\omega_1 = \sqrt{\frac{K_{eff}}{M_{eff}}}$, $\zeta_1 = \frac{C_{eff}}{2M_{eff}\omega_1}$, $\tau = \omega_1 t$, $()' = d/d\tau$, $\mu = \frac{\rho D^2 H}{2M_{eff}}$, $\theta = \frac{\Theta_1}{M_{eff}\omega_1^2 D}$, $S_n = 2\pi S_t$, $u = \frac{\omega_{VIV}}{\omega_1} = \frac{2\pi US_t}{\omega_1 D}$, $x = \frac{q_1}{D}$, $m^* = \frac{D}{H + 0.5D}$

Eqs. (11) (15) and (16) can be normalized as follows.

$$x'' + \left[2\zeta_1 + \mu(f - A_1)\frac{u}{S_n}\right]x' - \sum_{i=3}^{7}\mu A_i\left(\frac{S_n}{u}\right)^{i-2}(x')^i + x + \theta V = -\mu f\psi\left(\frac{u}{S_n}\right)^2 \tag{17}$$

$$\psi'' + 2\zeta u\left[\left(\frac{2f}{C_{L0}}\right)^2\psi^2 - 1\right]\psi' + u^2\psi = -m^* x'' - uS_n x' \tag{18}$$

$$V' = \frac{\Theta_1 D}{C_p}x' - \frac{V}{RC_p\omega_1} \tag{19}$$

It is seen that the galloping force coefficients $A_i(i = 1, 3, 5, 7\cdots)$ determine the dynamic behavior of the galloping vibration of the energy scavenger, according to Eq. (17). Thus, it can be predicted that changes in the shapes of the bluff bodies change A_i and may significantly influence the galloping vibration of the energy scavenger. In Eq. (18), for the wind speed U, the normalized VIV frequency $u = \omega_{VIV}/\omega_1$ is proportional to the Strouhal number S_t, which is the characteristic value of the VIV. Based on the definition of Strouhal number, the larger Strouhal number leads to the faster vortex shedding. Moreover, it can also be predicted that designing the shape of the bluff body to increase S_t may easily activate the VIV of the energy scavenger at the low wind speed region, whereas the VIV would occur in the high wind speed region for the smaller Strouhal number.

3.2. Experimental validation

To validate the aforementioned mathematical model (Eqs. (17)-(19)), both the simulation and experimental results of the three cases in Fig. 1 for a wide range of wind speeds is presented in Fig. 3. The cases are BB1 $\alpha = 0^\circ$, BB2 $\alpha = 0^\circ$, BB3 $\alpha = 0^\circ$, cuboid bluff body and circular cylinder bluff body, which present the typical responses in the following analysis. The geometrical and physical parameters of the experimental prototype are presented in Table 1. The first-mode damping ratio ζ_1 and first-mode natural frequency ω_1 are determined through the force-free vibration experiment of the energy scavenger's beam structure. The aerodynamic coefficients of both the galloping vibration and VIV for simulation of the four cases are presented in Table 2, which are the rounded value close to the experimentally identified aerodynamic parameters. The load resistor (i.e. the input interface of the digital oscilloscope) is measured to be $R \approx 1.05$ MΩ. The air density $\rho = 1.208$ kg/m^3.

Fig. 3 presents both the simulation and experimental results of the RMS voltage output of the energy scavenger for the selected cases in $U = 1.0$ 4.5 m/s. Both Fig. 3 (a) and (b) show that both the simulation and experimental results are in a good agreement, which verifies the fidelity of the present mathematical model. It is also seen that for the cases "BB1 $\alpha = 0^\circ$" and "BB2 $\alpha = 0^\circ$", the Strouhal number S_t is smaller than that of the cases "BB3 $\alpha = 0^\circ$", and consequently the VIV of "BB1 $\alpha = 0^\circ$" and "BB2 $\alpha = 0^\circ$" need higher wind speed to activate. The VIV (the hump area in the voltage output) is located in the higher wind speed ($U > 2.5$ m/s), and consequently the energy scavenger exhibits both the galloping vibration and VIV. It is seen that for "BB3 $\alpha = 0^\circ$", the Strouhal number S_t is significantly larger than the other two cases, and therefore the VIV does not occur at the high wind speed. Instead, for the given range of the wind speeds, the energy scavenger mainly exhibits different types of the galloping vibration due to different galloping force coefficients A_i. This phenomenon corresponding to the changes in the Strouhal number S_t will be explained by using the

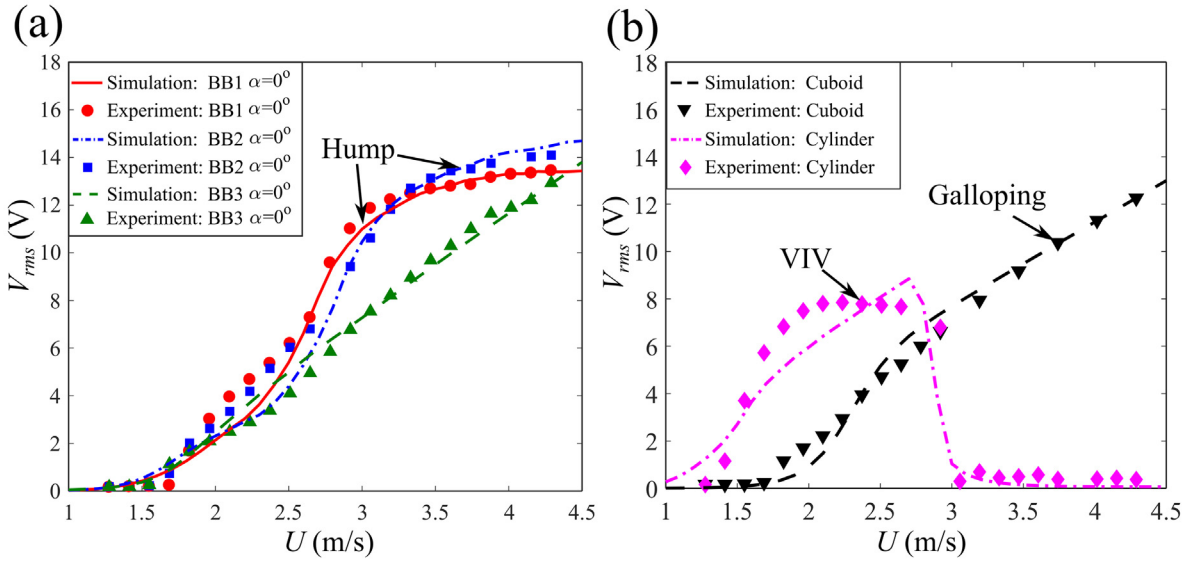

Fig. 3. The simulation and experimental results of the RMS voltage output of the energy scavenger for different bluff bodies: (a) BB1 $\alpha = 0^{\circ}$, BB2 $\alpha = 0^{\circ}$ and BB3 $\alpha = 0^{\circ}$; (b) the cuboid and cylinder bluff bodies.

Table 1
The geometrical and physical parameters of the experimental prototype.

Properties	Value
M_{eff}(kg)	4.1945×10^{-3}
ζ_1	0.013
ω_1(rad/s)	47.98
Θ_1(N/V)	4.95×10^{-5}
C_p(nF)	30.5

Table 2
The aerodynamic coefficients for typical cases.

Testing case	A_1	A_3	A_5	A_7	S_t	f	C_{L0}
BB1 $\alpha = 0^{\circ}$	4.9	−90	−60000	30,000	0.060	2.1	1.8
BB2 $\alpha = 0^{\circ}$	4.9	−90	−60000	30,000	0.055	2.1	1.8
BB3 $\alpha = 0^{\circ}$	3.2	−90	−1000	30,000	0.125	5.8	0.2
Cuboid	2	−90	−500	30,000	/	0	/
Cylinder	0	600	−25000	30,000	0.2	6.5	0.3

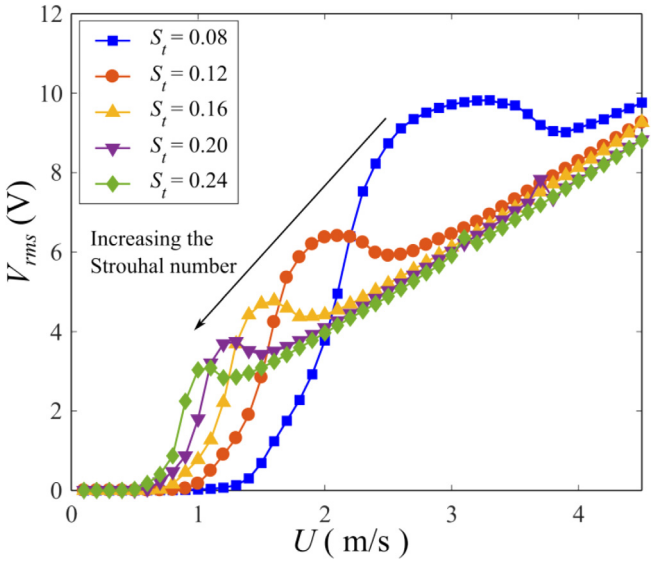

Fig. 4. The simulation results of the RMS voltage output of the energy scavenger corresponding to different Strouhal numbers S_t = [0.08, 0.12, 0.16, 0.20, 0.24].

simulation.

Apart from the results related to the proposed bluff bodies, the simulation and experimental results related to the conventional cuboid and cylinder bluff bodies are also presented in Fig. 3 (b). It is seen that in Table 2, $f = 0$ for the cuboid bluff body, and consequently the energy scavenger only exhibits galloping as shown in Fig. 3 (b) due to removing the VIV equation effect (i.e., $-\mu f\psi(u/S_n)^2 = 0$ in Eq. (17) and the whole Eq. (18)). Moreover, when setting the galloping force coefficients $A_1 = 0$, the energy scavenger exhibits the VIV for the circular cylinder bluff body, which also agrees well with the experimental results.

To explain the function of the Strouhal number S_t in coupled galloping and VIV of the energy scavenger, Fig. 4 presents the RMS voltage output of the energy scavenger corresponding to five different Strouhal numbers S_t = [0.08, 0.12, 0.16, 0.20, 0.24]. The other aerodynamic parameters are the same as in the case "BB1 $\alpha = 0^{\circ}$". The results show that for the smaller Strouhal number (e.g. $S_t = 0.08$), the hump area due to the VIV exists in the high wind speed (e.g. $U > 2$ m/s). When increasing S_t, the hump area moves towards the lower wind speed, and the hump becomes more significant. This indicates that for the larger S_t, the energy scavenger would exhibit more significant VIV for the lower wind speed. According to Eq. (18), u determines the lock-in frequency of the VIV wake oscillator equation (i.e. the term $u^2\psi$). That is, the VIV can be activated for a certain range of u, which behaves like a 'resonance phenomenon'. The definition of $u = 2\pi S_t U/\omega_1 D_2$ indicates that to activate the VIV (which is determined by the certain range of u), lower wind speed U is required for a higher value of Strouhal number S_t. Therefore, higher S_t can move the hump area (i.e. the VIV) to the lower wind speed U. Thus, the simulation results show that changing the aerodynamic coefficients by using the appropriate shape of the bluff body can enhance the performance of the coupled galloping vibration and VIV, i.e., improving the energy scavenger performance. It is also seen that higher Strouhal number reduces the wind speeds that activate the VIV, which is beneficial to reduce the threshold wind speed. Smaller Strouhal number leads to a hump area in the higher wind speed, which improves the voltage output at these wind speeds.

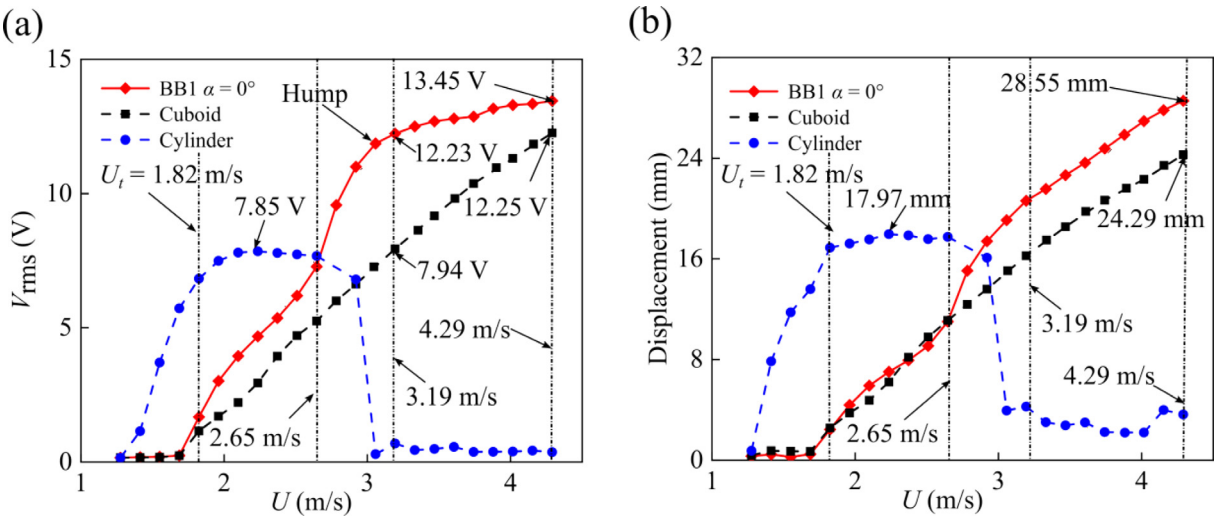

Fig. 5. Performance comparison between the energy scavenger with "BB1 $\alpha = 0^{\circ}$", cuboid and cylinder bluff bodies (a) RMS voltage output (b) RMS vibration displacement of the bluff body.

4. Experimental results and discussion

4.1. Performance of the energy scavenger with the BB1 bluff body

Fig. 5 (a) and (b) present the performance of the energy scavenger with "BB1 $\alpha = 0^{\circ}$", the cuboid and cylinder bluff bodies. In Fig. 5 (a), one can see that the performance is enhanced compared to the conventional energy scavenger with the cuboid bluff body (which only exhibits the galloping) for the investigated range of wind speeds. For "BB1 $\alpha = 0^{\circ}$", the maximum value of the voltage output reached 13.45 V, which is 9.8% higher than that of the cuboid case (12.25 V). By comparing with the effective threshold wind speed of energy scavenging U_t (the smallest wind speed to activate the energy scavenger vibration), the threshold wind speed of "BB1 $\alpha = 0^{\circ}$" does not vary. For "BB1 $\alpha = 0^{\circ}$", the energy scavenger firstly exhibits the galloping. Afterward, it is worth noting that as the wind speed gets higher, for the voltage output response, the VIV is observed from $U = 2.646$ m/s, and the hump area is generated. However, similar performance is not found in the displacement response curve. This phenomenon occurs because the vibrational frequency is enhanced due to the VIV, which will be interpreted in the following section in detail. It can be summarized that comparing to the conventional energy scavenger with the cuboid bluff body, "BB1 $\alpha = 0^{\circ}$" can enhance the energy scavenging performance by improving 9.80% of the maximum voltage output. Particularly, for $U = 3.194$ m/s in the hump area, due to the VIV, the voltage output of "BB1 $\alpha = 0^{\circ}$" is 53.93% higher than the cuboid case, which significantly enhances the energy scavenging performance.

Comparing "BB1 $\alpha = 0^{\circ}$" and the conventional energy scavenger with the circular cylinder bluff body (which only exhibits the VIV), it is seen that in the low wind speed region ($U < 2.65$ m/s), the energy scavenger with the circular cylinder bluff body produces a higher voltage output and has a lower threshold wind speed than "BB1 $\alpha = 0^{\circ}$". However, when the wind speed is improved to be $U > 3$ m/s, the VIV of the energy scavenger with the circular cylinder bluff body elapses, resulting in no power output. In contrast, the vibration of "BB1 $\alpha = 0^{\circ}$" still exists, which continuously produces a significant voltage output. Thus, on the perspective view of the broadband energy scavenging, "BB1 $\alpha = 0^{\circ}$" outperforms the conventional energy scavenger with the cuboid bluff body (only galloping) and the circular cylinder bluff body (only VIV), by bringing together the advantages of both the galloping and VIV.

Fig. 6 (a) and (b) compare the voltage outputs and displacement responses of "BB1 $\alpha = 90^{\circ}$", the cuboid and cylinder bluff bodies. For "BB1 $\alpha = 90^{\circ}$", it is seen that low-wind-speed VIV (the unshaded area) can be observed which leads to a lower threshold wind speed of energy scavenging (i.e. $U_t = 1.55$ m/s compared to the cuboid bluff body $U_t = 1.82$ m/s), and then the VIV is transited into galloping. In the VIV region of the "BB1 $\alpha = 90^{\circ}$", the higher voltage output and vibration amplitude are produced than the conventional cuboid bluff body, which indicates the energy scavenging enhancement. However, in the galloping region (the shaded area in Fig. 6 (a) and (b)), the performance of energy scavenging is degraded in terms of the voltage output and displacement, both of which are lower than the conventional energy scavenger with the cuboid bluff body. By comparing "BB1 $\alpha = 90^{\circ}$" with the circular cylinder bluff body, it is also seen that "BB1 $\alpha = 90^{\circ}$" is outperformed by the energy scavenger with the circular cylinder bluff body in the low wind speed ($U < 3$ m/s), although "BB1 $\alpha = 90^{\circ}$" generates higher voltage output in the high wind speed ($U > 3$ m/s) owing to the galloping. In summary, the performance of "BB1 $\alpha = 90^{\circ}$" is not as good as the conventional energy scavenger with the cuboid bluff body in a wide range of speed and with the circular cylinder bluff body in the low wind speed.

4.2. The analysis of the hump phenomenon

To further explain the "hump" phenomenon of "BB1 $\alpha = 0^{\circ}$" in Fig. 5, Fig. 7 (a-d) comprehensively present the time history and the frequency response of the "BB1 $\alpha = 0^{\circ}$" and the cuboid bluff body subjected to the wind speed 3.194 m/s in terms of the voltage output and displacement, respectively. It can be found that in Fig. 7 (a) and (c) that there exist two different frequencies of voltage output and the displacement, which are 8.30 Hz and 6.17 Hz, respectively. That is, even though the vibration displacement of the energy scavenger with "BB1 $\alpha = 0^{\circ}$" is not significantly larger than the that of the energy scavenger with the cuboid bluff body in the "hump area" (2.65 m/s $\leq U \leq$ 4.29 m/s), the vibrational velocity of the energy scavenger with "BB1 $\alpha = 0^{\circ}$" is enhanced significantly, i.e., the vibration becomes more quickly due to increased vibration frequency (i.e., 6.17 Hz is increased to be 8.30 Hz). According to Eq. (17), the voltage output V and vibration velocity x' satisfy

$$|V| = \frac{\Theta_1 DR\omega_1}{\sqrt{R^2 C_p^2 \omega_1^2 \sigma^2 + 1}} |\dot{x}| \tag{20}$$

where $|V|$ and $|\dot{x}|$ are the amplitudes of the voltage output V and the vibration velocity x' at the normalized vibration frequency σ, respectively. It is seen that $|V|$ is proportional to the energy scavenger vibration velocity $|\dot{x}|$ instead of the displacement, and therefore the improved

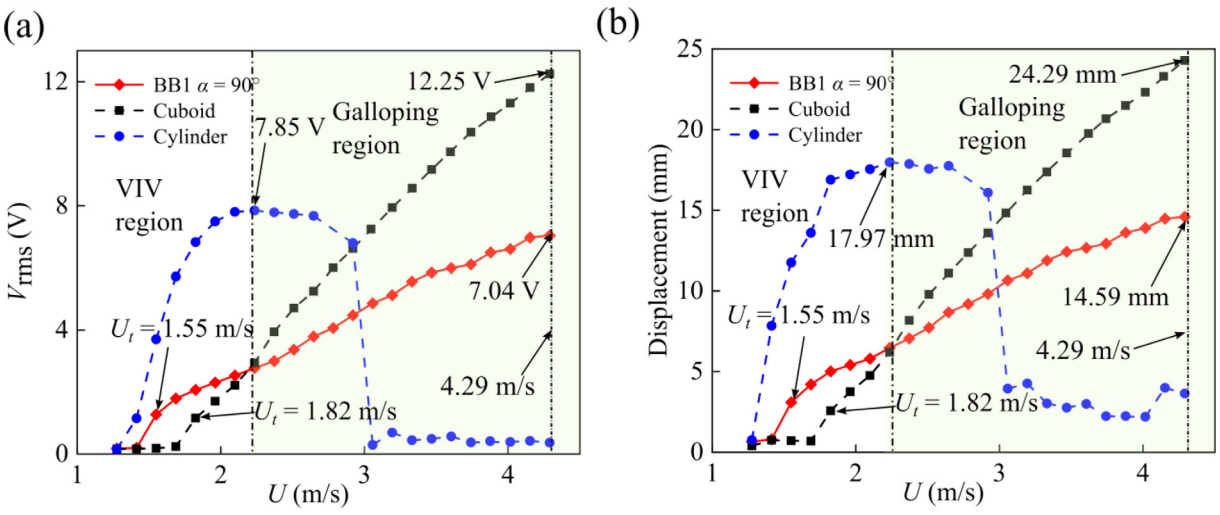

Fig. 6. Performance comparison of the energy scavenger with the different bluff bodies: (a) RMS voltage output and (b) RMS vibration displacement for "BB1 $\alpha = 90^{\circ}$", cuboid and cylinder bluff bodies.

vibration velocity $|\dot{x}|$ leads to voltage output enhancement. This agrees well with the experimental observations in Fig. 5, which shows that the "hump" exists in the voltage output curve instead of the vibration displacement curve.

4.3. Comprehensive study of the flow patterns

To better explain the mechanism of the influence of combining shape on the aerodynamic response, a comprehensive CFD study has been conducted on XFlow (Dassault, co.,), a lattice Boltzmann method

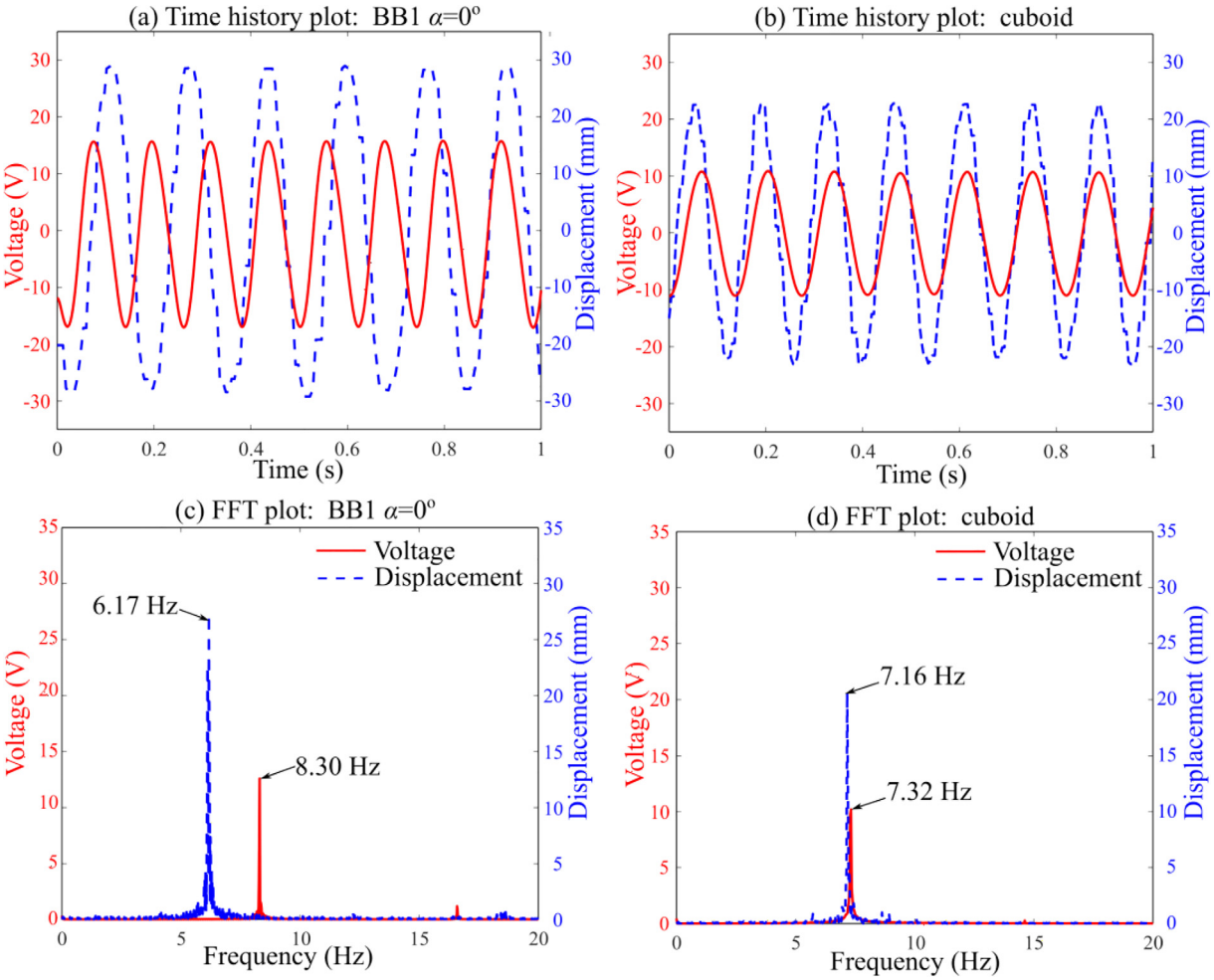

Fig. 7. Experimental time history and FFT plots of the energy scavenger with the different bluff bodies for the wind speed 3.194 m/s: (a) (c) BB1 $\alpha = 0^{\circ}$; (b) (d) cuboid.

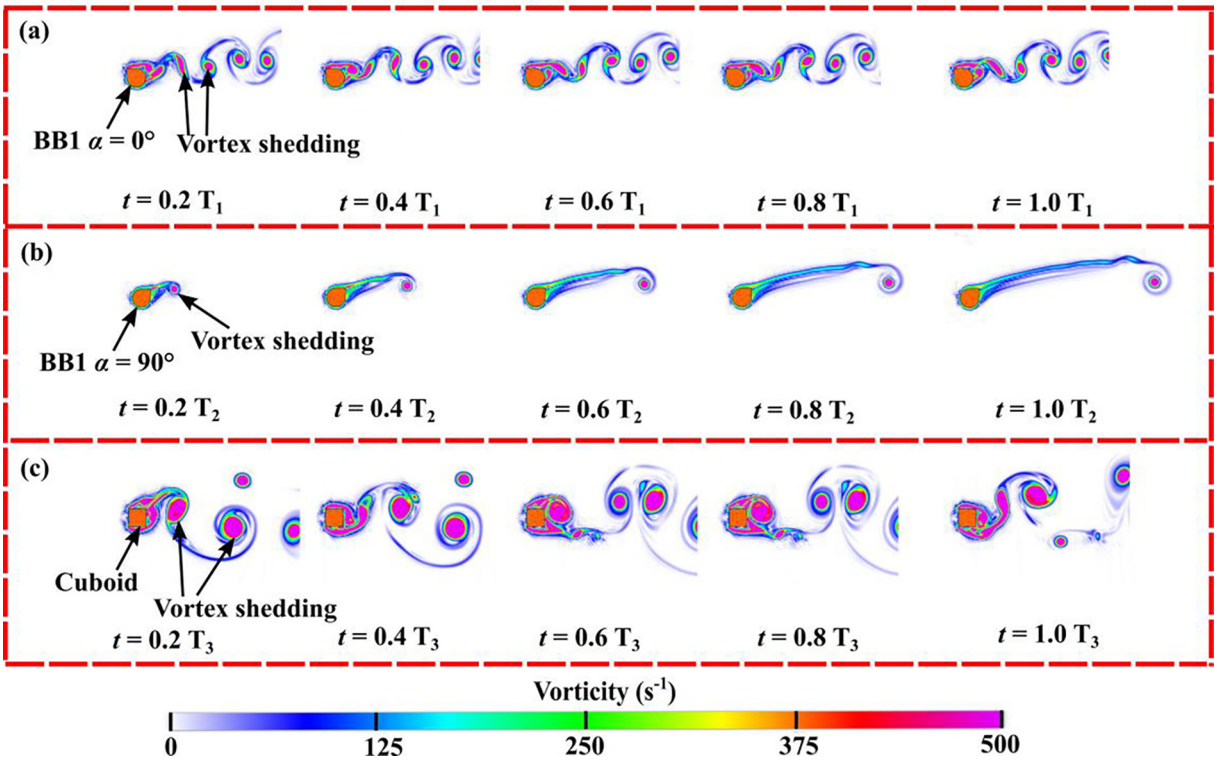

Fig. 8. The synergy effect of vortex shedding progress with energy scavenging performance of (a) BB1 $\alpha = 90^{\circ}$, (b) cuboid and (c) BB2.$\alpha = 0^{\circ}$.

based CFD platform [61]. Three typical cases are selected to show the synergy effect of vortex shedding progress for energy scavenging performance, as shown in Fig. 8 (a)-(c). In the figure, T_i (i = 1, 2, 3) is the Strouhal vortex shedding period corresponding to each bluff body. By comparing with "BB1 $\alpha = 0^{\circ}$" and "BB1 $\alpha = 90^{\circ}$" in Fig. 8 (a)-(b), the structures respectively strengthen and weaken the energy scavenging performance which is also discovered in Fig. 5 and Fig. 6. Besides, for "BB1 $\alpha = 0^{\circ}$" the vortex shedding process is shown in the pattern of "P + S" [62]. However, for "BB1 $\alpha = 90^{\circ}$" the vortex shedding process was quite weak and represented as a jet flow, which illustrates that the structure is beneficial for anti-drag and suppressing but not enhancing the vibration. Thus, "BB1 $\alpha = 90^{\circ}$" is unbeneficial for energy scavenging. Fig. 8 (c) presents a typical 2P vortex shedding pattern of the cuboid bluff body, which means that comparing with "BB1 $\alpha = 90^{\circ}$" in Fig. 8 (b), the vortex shedding becomes more violent which leads to a more intensive energy scavenging performance. Furthermore, for "BB1 $\alpha = 0^{\circ}$" (the case with optimal overall performance) in Fig. 8 (a), it is interesting to see that the vortex shedding process becomes faster and sequential. This produces a significant pressure difference around the bluff body. As a result, the vibration of the bluff body is enhanced due to such an air-instability phenomenon, leading to the effectively enhanced energy scavenging performance.

4.4. Performance of the energy scavenger with the BB2 and BB3 bluff bodies

Fig. 9 (a) and (b) compare the RMS voltage outputs of the energy scavenger with the BB2 and BB3 bluff bodies for the different incoming attack angles α. For performance comparison, the results of the energy scavenger with the cuboid and cylinder bluff bodies are also presented as the benchmarks. As shown in Fig. 9 (a), the performance of "BB2 $\alpha = 0^{\circ}$" is similar to that of "BB1 $\alpha = 0^{\circ}$" in Fig. 5 (a). That is, the energy scavenger firstly enters into the galloping region, and then the VIV is occurred, which results in a sudden rise of the voltage output (i.e., the hump area). This indicates that "BB2 $\alpha = 0^{\circ}$" can produce significantly higher voltage output than the cuboid bluff body in a wide range of wind speeds. Likewise, the "BB2 $\alpha = 0^{\circ}$" outperforms the energy scavenger with the circular cylinder bluff body for the higher wind speed ($U > 3$ m/s). For other wind attack angles of the BB2 ("BB2 $\alpha = 90^{\circ}$ and 180°"), the voltage outputs are degraded compared to the energy scavenger with the cuboid bluff body in a wide range of wind speeds and with the circular cylinder bluff body in the low wind speed. Besides, "BB2 $\alpha = 180^{\circ}$" is significantly worse than that of "BB2 $\alpha = 0^{\circ}$ and 90°". This indicates that the different attack angles significantly influence the vibration behaviors of the energy scavenger with the BB2 bluff body, which leads to the different energy scavenging performance, although the cross-section is the same. As shown in Fig. 9 (b), likewise, in the low wind speed region ($U < 3$ m/s), the energy scavenger with the circular cylinder bluff body (which only exhibits the VIV) outperforms "BB3 $\alpha = 0^{\circ}$, 90°" and cuboid bluff body case. For the higher wind speed ($U > 3$ m/s), the energy scavenger with the circular cylinder bluff body does not generate any voltage output due to the elapse of the VIV to the high wind speed region. Compared to the energy scavenger with the cuboid bluff body (which only exhibits the galloping), for a wide range of wind speeds, "BB3 $\alpha = 0^{\circ}$" only slightly outperforms the cuboid bluff body, whereas "BB3 $\alpha = 90^{\circ}$" significantly degrades the performance. Therefore, based on the experimental results shown in Fig. 9, it can be summarized that "BB2 $\alpha = 0^{\circ}$" is beneficial to enhancing energy scavenging performance by significantly improving the voltage output for a wide range of wind speeds.

4.5. Summary of the experimental results

To clearly show the performance of the energy scavenger with the different designed bluff bodies, this subsection summarizes the crucial results of the experiment. Fig. 10 presents the performance enhancement percentages of the energy scavenger with BB1, BB2, and BB3 in terms of the maximum voltage output, respectively. The performance enhancement percentage of the maximum voltage output is defined as P_V, which satisfies

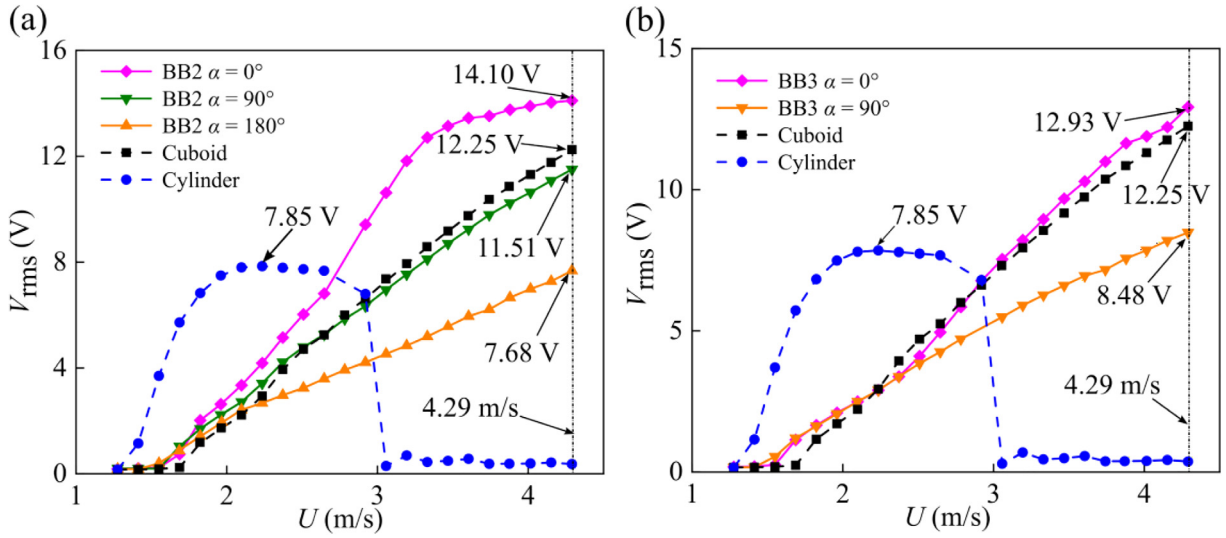

Fig. 9. Performance comparison of the energy scavenger with "BB2 $\alpha = 0^{\circ}, 90^{\circ}, 180^{\circ}$" and the cuboid bluff body: (a) RMS voltage output and (b) vibration displacement.

$$P_V = \frac{V_{tb} - V_{tc}}{V_{tc}} \times 100\% \tag{21}$$

where V_{tc}, V_{tb} are maximum voltage outputs of the counterpart (the cuboid and cylinder bluff bodies) and the tested bluff body in the experiment, respectively.

Fig. 10 (a) presents the performance comparison between the BB1 ~ BB3 bluff bodies subjected to different wind attack angles and the cuboid bluff body, while Fig. 10 (b) presents the performance comparison between the BB1 ~ BB3 bluff bodies and the circular cylinder bluff body. As shown in Fig. 10 (a), the results show that all the BB1 ~ BB3 outperform the cuboid-like galloping energy scavenger for $\alpha = 0^{\circ}$, where the maximum percentage is $P_V = 15.1\%$ for "BB2 $\alpha = 0^{\circ}$". For other wind attack angles except $\alpha = 0^{\circ}$, the energy scavenger with the BB1 ~ BB3 bluff bodies degrade the energy scavenging performance, where $P_V < 0$. This indicates that all the BB1 ~ BB3 subjected to $\alpha = 0^{\circ}$ is beneficial to energy scavenging compared with the galloping-based energy scavenger (with the cuboid bluff body). As shown in Fig. 10 (b), it is seen that all the cases except "BB1 $\alpha = 90^{\circ}$" can outperform the VIV-based energy scavenger (with the circular cylinder bluff body). BB1 ~ BB3 subjected to $\alpha = 0^{\circ}$ can improve the maximum voltage output by 71.34%, 79.62%, and 64.71%, respectively. Thus, the results show that BB1 ~ BB3 subjected to $\alpha = 0^{\circ}$ are favorable for significant performance enhancement, compared with both the galloping-based and VIV-based energy scavengers, and "BB2 $\alpha = 0^{\circ}$" is the optimal case among them due to its maximal improvement.

5. Conclusions

This paper investigates various cross-sectioned bluff bodies, which are constituted as a combination of circular- and cuboid foams for performance enhancement of a piezoelectric wind energy scavenger. It has been shown that the appropriate combinations of the circular and cuboid foams can activate both the vortex-induced vibration (VIV) and galloping of the energy scavenger simultaneously, which can significantly improve the wind energy scavenging performance. Through the theoretical analysis based on mathematical modeling, CFD simulations and experimental investigations, the following crucial conclusions are obtained.

a. A mathematical model that considers both the VIV and galloping of the energy scavenger is experimentally validated. The theoretical

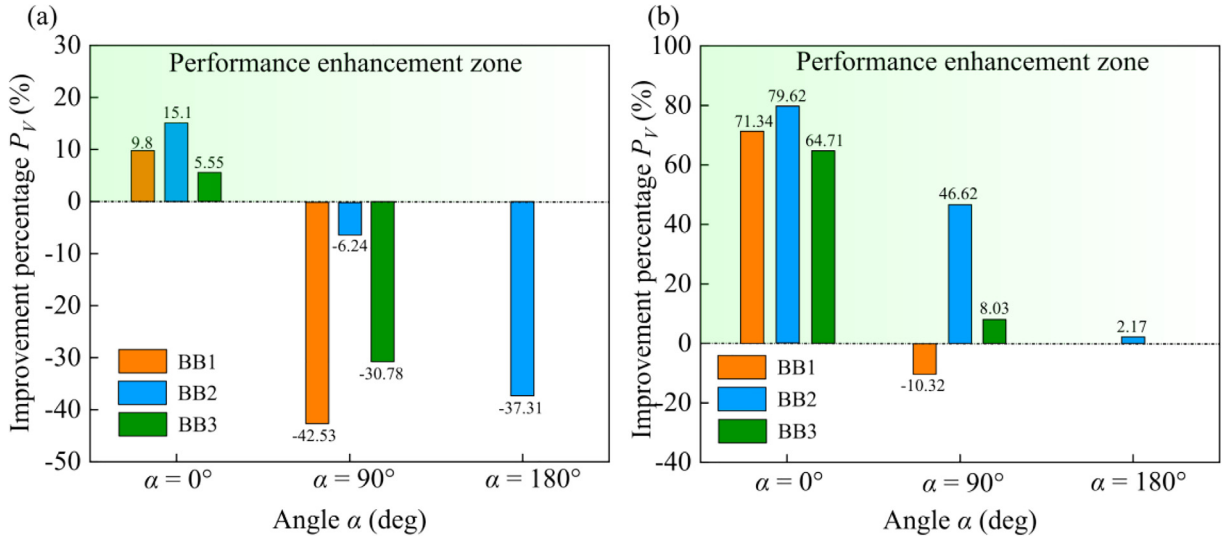

Fig. 10. The performance enhancement percentages of the energy scavenger with BB1, BB2, and BB3 in terms of the maximum voltage output compared with (a) the cuboid bluff body and (b) the circular cylinder bluff body.

analysis based on the mathematical model reveals that different Strouhal number values and galloping aerodynamic force coefficients significantly influence the performance trend corresponding to the changes in the wind speed. Higher Strouhal number reduces the wind speeds that activate the VIV, which is beneficial for reducing the threshold wind speed. Lower Strouhal number leads to the hump area in the higher wind speed region, which improves the voltage output within this region.

b. Through experimental performance comparison with the conventional cuboid and cylinder bluff bodies, this study reveals that both the appropriate cross-section design and the attack angles play a key role in the device's performance enhancement. With the appropriate cross-section and wind attack angles ("BB1 $\alpha = 0^{\circ}$" and "BB2 $\alpha = 0^{\circ}$"), both the advantages of the galloping and VIV are brought together, which shows a special "hump" phenomenon, leading to significant energy scavenging enhancement. For example, compared to the case that only exhibits galloping or VIV, "BB1 $\alpha = 0^{\circ}$" can achieve 9.8% or 71.34% improvement of the maximum voltage output. Particularly for some wind speed values in the hump phenomenon area, the voltage output can increase by 53.93% compared to the galloping only case.

c. The CFD numerical simulations of "BB1 $\alpha = 0^{\circ}$", "BB1 $\alpha = 90^{\circ}$" and the conventional cuboid bluff body are performed as the examples for interpreting the physical mechanism. The results show that the three bluff bodies exhibit different vortex shedding effects. For the "BB1 $\alpha = 0^{\circ}$", it is found that the vortex shedding is demonstrating a "P + S" pattern, which produces a significant pressure difference around the bluff body. But for the "BB1 $\alpha = 90^{\circ}$", the bluff body significantly weakens the vortex shedding process. Therefore, the vibration of the bluff body is enhanced due to such an air-instability phenomenon (significant pressure difference), and consequently, the energy scavenging performance is effectively enhanced.

CRediT authorship contribution statement

Junlei Wang: Writing - original draft, Software, Methodology, Conceptualization. **Shanghao Gu:** Data curation, Formal analysis, Investigation. **Chengyun Zhang:** Data curation, Formal analysis. **Guobiao Hu:** Writing - review & editing. **Geng Chen:** Software. **Kai Yang:** Methodology, Supervision, Writing - review & editing. **Hang Li:** Software. **Yuyang Lai:** Software. **Grzegorz Litak:** Funding acquisition. **Daniil Yurchenko:** Methodology.

Declaration of Competing Interest

The authors declare that they have no known competing financial interests or personal relationships that could have appeared to influence the work reported in this paper.

Acknowledgments

This work was supported by National Natural Science Foundation of China (Grant No.: 51977196 and 11802097). GL was supported by the Polish Ministry of Science and Higher Education under the project fx1DIALOG 0019/DLG/2019/10 in the years 2019-2021.

References

[1] Kumar S, Singh HH, Khare N. Flexible hybrid piezoelectric-thermoelectric generator for harnessing electrical energy from mechanical and thermal energy. Energy Convers Manage 2019;198:111783.
[2] Kim TY, Kwak J, Kim B-W. Application of compact thermoelectric generator to hybrid electric vehicle engine operating under real vehicle operating conditions. Energy Convers Manage 2019;201:112150.
[3] Maamer B, Boughamoura A, El-Bab AMF, Francis LA, Tounsi F. A review on design improvements and techniques for mechanical energy harvesting using piezoelectric and electromagnetic schemes. Energy Convers Manage 2019;199:111973.
[4] Qasem NA, Ahmed M, Zubair SM. The impact of thermodynamic balancing on performance of a desiccant-based humidification-dehumidification system to harvest freshwater from atmospheric air. Energy Convers Manage 2019;199:112011.
[5] Van Toan N, Hasnan MMIM, Udagawa D, Inomata N, Toda M, Said SM, et al. Thermoelectric power battery using al2o3 nanochannels of 10 nm diameter for energy harvesting of low-grade waste heat. Energy Convers Manage 2019;199:111979.
[6] Zhao L-C, Zou H-X, Yan G, Liu F-R, Tan T, Wei K-X, et al. Magnetic coupling and flextensional amplification mechanisms for high-robustness ambient wind energy harvesting. Energy Convers Manage 2019;201:112166.
[7] Lai Z, Wang J, Zhang C, Zhang G, Yurchenko D. Harvest wind energy from a vibro-impact deg embedded into a bluff body. Energy Convers Manage 2019;199:111993.
[8] Guo X, Zhang Y, Fan K, Lee C, Wang F. A comprehensive study of non-linear air damping and "pull-in" effects on the electrostatic energy harvesters. Energy Convers Manage 2020;203:112264.
[9] Zuo W, Li J, Zhang Y, Li Q, Jia S, He Z. Multi-factor impact mechanism on combustion efficiency of a hydrogen-fueled micro-cylindrical combustor. Int J Hydrogen Energy 2020;45(3):2319–30.
[10] Zou H-X, Zhang W-M, Li W-B, Wei K-X, Gao Q-H, Peng Z-K, et al. Design and experimental investigation of a magnetically coupled vibration energy harvester using two inverted piezoelectric cantilever beams for rotational motion. Energy Convers Manage 2017;148:1391–8.
[11] Fan K, Cai M, Wang F, Tang L, Liang J, Wu Y, et al. A string-suspended and driven rotor for efficient ultra-low frequency mechanical energy harvesting. Energy Convers Manage 2019;198:111820.
[12] Zou H-X, Zhao L-C, Gao Q-H, Zuo L, Liu F-R, Tan T, et al. Mechanical modulations for enhancing energy harvesting: principles, methods and applications. Appl Energy 2019;255:113871.
[13] Yu K, Liang J, Qu B, Chen X, Wang H. Parameters identification of photovoltaic models using an improved jaya optimization algorithm. Energy Convers Manage 2017;150:742–53.
[14] Zuo W, Li Q, He Z, Li Y. Numerical investigations on thermal performance enhancement of hydrogen-fueled micro planar combustors with injectors for micro-thermophotovoltaic applications. Energy 2020;194:116904.
[15] Fan K, Zhang Y, Tang L, Qu H. A string-driven rotor for efficient energy harvesting from ultra-low frequency excitations. Appl Phys Lett 2019;115(20):203903.
[16] Zhao X, Cai J, Guo Y, Li C, Wang J, Zheng H. Modeling and experimental investigation of an aa-sized electromagnetic generator for harvesting energy from human motion. Smart Mater Struct 2018;27(8):085008.
[17] Yang Z, Tang L, Yu L, Tao K, Aw K. Modelling and analysis of an out-of-plane electret-based vibration energy harvester with ac and dc circuits. Mech Syst Sig Process 2020;140:106660.
[18] Tao K, Yi H, Yang Y, Chang H, Wu J, Tang L, et al. Origami-inspired electret-based triboelectric generator for biomechanical and ocean wave energy harvesting. Nano Energy 2019:104197.
[19] Zhang L, Meng B, Xia Y, Deng Z, Dai H, Hagedorn P, et al. Galloping triboelectric nanogenerator for energy harvesting under low wind speed. Nano Energy 2020:104477.
[20] Sodano HA, Park G, Inman D. Estimation of electric charge output for piezoelectric energy harvesting. Strain 2004;40(2):49–58.
[21] Erturk A, Inman DJ. Piezoelectric energy harvesting. John Wiley & Sons; 2011.
[22] Fang S, Fu X, Du X, Liao W-H. A music-box-like extended rotational plucking energy harvester with multiple piezoelectric cantilevers. Appl Phys Lett 2019;114(23):233902.
[23] Wang J, Geng L, Ding L, Zhu H, Yurchenko D. The state-of-the-art review on energy harvesting of flow-induced vibrations. Appl Energy 2020;267:114902.
[24] Chen Z, Xia Y, He J, Xiong Y, Wang G. Elastic-electro-mechanical modeling and analysis of piezoelectric metamaterial plate with a self-powered synchronized charge extraction circuit for vibration energy harvesting. Mech Syst Sig Process 2020;143:106824.
[25] Lu Z, Chen L-Q, Brennan MJ, Yang T, Ding H, Liu Z. Stochastic resonance in a nonlinear mechanical vibration isolation system. J Sound Vib 2016;370:221–9.
[26] Hu G, Wang J, Su Z, Li G, Peng H, Kwok K. Performance evaluation of twin piezoelectric wind energy harvesters under mutual interference. Appl Phys Lett 2019;115(7):073901.
[27] Wang J, Hu G, Su Z, Li G, Zhao W, Tang L, et al. A cross-coupled dual-beam for multi-directional energy harvesting from vortex induced vibrations. Smart Mater Struct 2019;28(12):12LT02.
[28] Zhu H, Yao J, Ma Y, et al. Simultaneous CFD evaluation of VIV suppression using smaller control cylinders. J Fluids Struct 2015;57:66–80.
[29] Le HD, Kwon S-D. An electromagnetic galloping energy harvester with double magnet design. Appl Phys Lett 2019;115(13):133901.
[30] Yan Z, Wang L, Hajj MR, Yan Z, Sun Y, Tan T. Energy harvesting from iced-conductor inspired wake galloping. Extreme Mech Lett 2020:100633.
[31] Yang Y-G, Sun Y-H, Xu W. Stochastic bifurcations of a fractional-order vibro-impact system driven by additive and multiplicative Gaussian white noises. Complexity 2019;2019:6737139.
[32] Huang D, Zhou S, Yang Z. Resonance mechanism of nonlinear vibrational multistable energy harvesters under narrow-band stochastic parametric excitations. Complexity 2019;2019:1050143.
[33] Wang J, Geng L, Yang K, et al. Dynamics of the double-beam piezo-magneto-elastic nonlinear wind energy harvester exhibiting galloping-based vibration. Nonlinear Dyn 2020. https://doi.org/1007/s11071-020-05633-3.
[34] Huang D, Zhou S, Han Q, Litak G. Response analysis of the nonlinear vibration energy harvester with an uncertain parameter. Proc Inst Mech Eng, Part K: J Multibody Dyn 2019.
[35] Allen J, Smits A. Energy harvesting eel. J Fluids Struct 2001;15(3–4):629–40.

[36] Akaydin HD, Elvin N, Andreopoulos Y. Energy harvesting from highly unsteady fluid flows using piezoelectric materials. J Intell Mater Syst Struct 2010;21(13):1263–78.
[37] Mehmood A, Hajj M, Nayfeh A, Akhtar I, Nuhait A. Piezoelectric energy harvesting from vortex-induced vibrations of circular cylinder. J Sound Vib 2013;332(19):4656–67.
[38] Dai H, Abdelkefi A, Wang L. Theoretical modeling and nonlinear analysis of piezoelectric energy harvesting from vortex-induced vibrations. J Intell Mater Syst Struct 2014;25(14):1861–74.
[39] Zhu H, Yao J. Numerical evaluation of passive control of VIV by small control rods. Appl Ocean Res 2015;51:93–116.
[40] Zhu H, Li G, Wang J. Flow-induced vibration of a circular cylinder with splitter plates placed upstream and downstream individually and simultaneously. Appl Ocean Res 2020;97:102084.
[41] Wang J, Zhou S, Zhang Z, Yurchenko D. High-performance piezoelectric wind energy harvester with y-shaped attachments. Energy Convers Manage 2019;181:645–52.
[42] Wang J, Tang L, Zhao L, Zhang Z. Efficiency investigation on energy harvesting from airflows in hvac system based on galloping of isosceles triangle sectioned bluff bodies. Energy 2019;172:1066–78.
[43] Gong Y, Shan X, Luo X, Pan J, Xie T, Yang Z. Direction-adaptive energy harvesting with a guide wing under flow-induced oscillations. Energy 2019;187:115983.
[44] Wang J, Tang L, Zhao L, Hu G, Song R, Xu K. Equivalent circuit representation of a vortex-induced vibration-based energy harvester using a semi-empirical lumped parameter approach. Int J Energy Res 2020;44(6):4516–28.
[45] Al Nuaimi SK, Meesala VC, Hajj MR. Phenomenological model of piezoelectric energy harvesting from galloping oscillations. Appl Phys Lett 2019;115(19):193701.
[46] Barrero-Gil A, Vicente-Ludlam D, Gutierrez D, Sastre F. Enhance of energy harvesting from transverse galloping by actively rotating the galloping body. Energies 2019;13(1):1–18.
[47] Abdelkefi A, Hajj M, Nayfeh A. Piezoelectric energy harvesting from transverse galloping of bluff bodies. Smart Mater Struct 2012;22(1):015014.
[48] Yang Y, Zhao L, Tang L. Comparative study of tip cross-sections for efficient galloping energy harvesting. Appl Phys Lett 2013;102(6):064105.
[49] Yan Z, Lei H, Tan T, Sun W, Huang W. Nonlinear analysis for dual-frequency concurrent energy harvesting. Mech Syst Sig Process 2018;104:514–35.
[50] Yan Z, Sun W, Tan T, Huang W. Nonlinear analysis of galloping piezoelectric energy harvesters with inductive-resistive circuits for boundaries of analytical solutions. Commun Nonlinear Sci Numer Simul 2018;62:90–116.
[51] Bibo A, Alhadidi AH, Daqaq MF. Exploiting a nonlinear restoring force to improve the performance of flow energy harvesters. J Appl Phys 2015;117(4):045103.
[52] Wang J, Geng L, Zhou S, Zhang Z, Lai Z, Yurchenko D. Design, modeling and experiments of broadband tristable galloping piezoelectric energy harvester. Acta Mech Sin 2019:1–14. https://doi.org/10.1007/s10409-020-00928-5.
[53] Yang K, Wang J, Yurchenko D. A double-beam piezo-magneto-elastic wind energy harvester for improving the galloping-based energy harvesting. Appl Phys Lett 2019;115(19):193901.
[54] Wang C, Zhang Q, Wang W, Feng J. A low-frequency, wideband quad-stable energy harvester using combined nonlinearity and frequency up-conversion by cantilever-surface contact. Mech Syst Sig Process 2018;112:305–18.
[55] Sun W, Guo F, Seok J. Development of a novel vibro-wind galloping energy harvester with high power density incorporated with a nested bluff-body structure. Energy Convers Manage 2019;197:111880.
[56] Tan T, Hu X, Yan Z, Zhang W. Enhanced low-velocity wind energy harvesting from transverse galloping with super capacitor. Energy 2019;187:115915.
[57] He X, Yang X, Jiang S. Enhancement of wind energy harvesting by interaction between vortex-induced vibration and galloping. Appl Phys Lett 2018;112(3):033901.
[58] Yang X, He X, Li J, Jiang S. Modeling and verification of piezoelectric wind energy harvesters enhanced by interaction between vortex-induced vibration and galloping. Smart Mater Struct 2019;28(11):115027.
[59] Sun W, Jo S, Seok J. Development of the optimal bluff body for wind energy harvesting using the synergetic effect of coupled vortex induced vibration and galloping phenomena. Int J Mech Sci 2019;156:435–45.
[60] Qin W, Deng W, Pan J, Zhou Z, Du W, Zhu P. Harvesting wind energy with bi-stable snap-through excited by vortex-induced vibration and galloping. Energy 2019;189:116237.
[61] Zhou S, Wang J. Dual serial vortex-induced energy harvesting system for enhanced energy harvesting. AIP Adv 2018;8(7):075221.
[62] Zou Q, Ding L, Wang H, Wang J, Zhang L. Two-degree-of-freedom flow-induced vibration of a rotating circular cylinder. Ocean Eng 2019;191:106505.